5th ECPMG Delft · 2024

Proceedings of the 5th ECPMG 2024
5th European Conference on Physical Modelling in Geotechnics
2-4 October 2024, Delft, the Netherlands

Effect of elastic modulus on masonry buildings during tunnelling: a coupled centrifuge-numerical modelling study

C. Tang & A. M. Marshall
Department of Civil Engineering, University of Nottingham, Nottingham NG7 2RD, UK,
chuanjin.tang@nottingham.ac.uk, alec.marshall@nottingham.ac.uk

ABSTRACT: In this study, a novel coupled centrifuge-numerical modelling (CCNM) approach of shallow strip foundations developed at the University of Nottingham Centre for Geomechanics (NCG) is used to study the response of masonry building behaviour during tunnelling. In the CCNM method, full-scale masonry walls are simulated using a concrete damage plasticity (CDP) constitutive model in Abaqus, while small-scale models of the strip foundation, tunnel, and soil are modelled in a geotechnical centrifuge at elevated gravity-levels (70 g); the foundation settlements in the centrifuge model are transferred in "real-time" to the base of the masonry wall in Abaqus, and subsequently, new loads at the building base (due to structural load redistribution) are fed back to the foundation model after the Abaqus calculation. This testing approach emphasises the crucial role of real-time redistribution of building stresses in tunnel-building interaction scenarios. The data presented in this paper focuses on the effect of the elastic modulus within the adopted CDP model. Initial test results provide valuable insights into how elastic modulus influences the deformation and damage patterns of masonry buildings, as well as the surface settlement profiles, during tunnelling activities.

1 INTRODUCTION

Tunnelling under masonry buildings with shallow strip foundations may threaten the building integrity. Therefore, it is crucial to understand the mechanisms of building damage induced by tunnel excavation.

Geotechnical centrifuge testing is a common and effective simulation method, as it can provide stress conditions comparable to full-scale scenarios. The results, however, are typically affected by model simplifications, for example, the use of plates (Farrell et al., 2014) and 3D-printed models (Ritter et al., 2020) to represent buildings. The replication of realistic deformation and load distributions within model buildings is difficult to obtain.

To further understand the tunnel-masonry building interaction mechanisms, this paper uses a new coupled centrifuge-numerical modelling (CCNM) approach (Tang et al., 2024) to study the effect of tunnelling under masonry buildings. The results presented in this paper are a subset of a larger experimental data set; this paper focuses on the effect of Young's modulus within the adopted concrete damage plasticity (CDP) model for masonry buildings. The tunnel and strip foundation are included in the centrifuge model (experimental domain), while the buildings are modelled in Abaqus (numerical domain); the two model domains share data through a LabVIEW data exchange interface. The tests were conducted in the Nottingham Centre for Geomechanics (NCG) centrifuge at 70 g (g is gravity).

2 EXPERIMENT SETUP

The test layout and experimental package originate from Tang et al. (2024). Figure 1 presents the test layout under plane strain conditions, representing a full-scale prototype scenario of a 6.3 m diameter tunnel (D_t=6.3 m) buried with a cover depth C of 8.19 m (C/D_t=1.3), where a masonry wall (with length L=20 m, height H=8.5 m, thickness 0.36 m, opening ratio O=19%) on a masonry strip foundation (20.79 m length × 2.66 m width × 0.36 m thickness) is located directly above the tunnel.

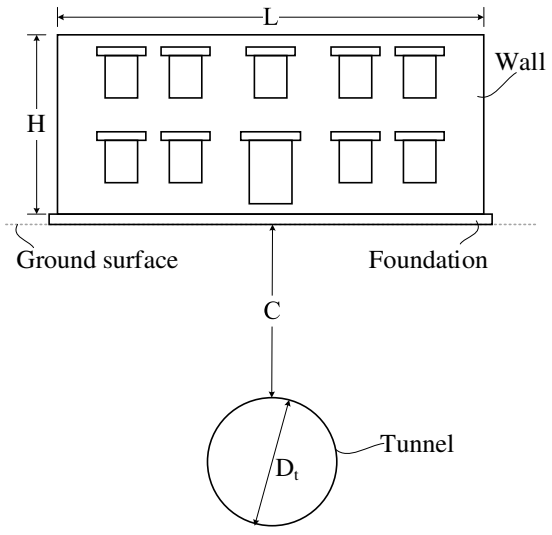

Figure 1. Test layout.

2.1 Centrifuge model

Figure 2 shows the centrifuge model package. The soil within the strongbox is dry Leighton Buzzard Fraction E silica sand, with an average grain size of 0.14 mm, a uniformity coefficient of 1.58, a specific gravity of 2.65, maximum/minimum void ratios of 1.01/0.61. An eccentric rigid boundary mechanical model tunnel (developed by Song et al. (2020)) was used to impose volume loss ($V_{l,t} \leqslant 3.5\%$). Two Dalsa Genie Nano-M4020 12.4 megapixel cameras were used to capture soil and strip foundation movements through the front transparent acrylic wall of the strongbox for digital image analysis (GeoPIV_RG; Stanier at al., 2016).

An aluminium strip foundation model, replicating the bending stiffness of a full (prototype) scale masonry strip foundation (i.e. 31 MN·m^2; Young's modulus of aluminium 70 GPa; masonry 3 GPa), was placed on the soil surface directly above the tunnel and close to the Perspex window. The foundation width in the tunnel longitudinal axis direction was 38 mm to provide enough space to install pneumatic cylinders (25 mm bore, 25 mm stroke, C85 series, double acting, maximum 1 MPa pressure) used for load application. Seven raised beams, with a length equal to the foundation width, were spaced at 47.5 mm intervals to evenly distribute loads (from the cylinders) across the foundation width. Cylinder rods, 500 N load cells, and rod end bearings were connected in line with the centre of the raised beams to apply and measure loads on the strip foundation. Seven 10 mm stroke linear variable differential transformers (LVDT) were used to acquire foundation settlements. The pressure within the lower chamber of each cylinder was linked to a unique compact electro-pneumatic regulator (ITV0050-3ML-Q, maximum 1 MPa pressure supply) through 4 mm diameter pipes, while all top chamber pressures were connected to a common regulator using a manifold; an air compressor supplied 950 kPa compressed air to the regulators.

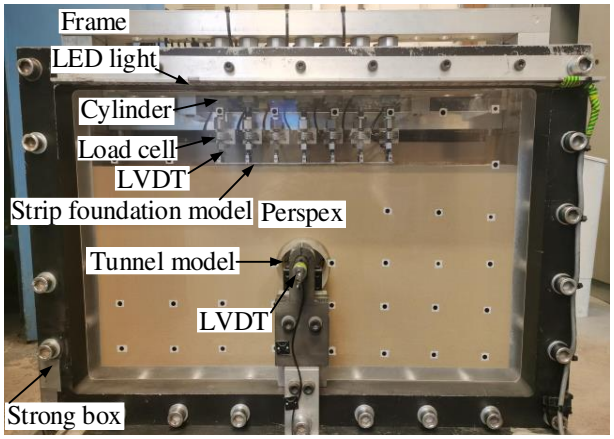

Figure 2. Centrifuge model.

2.2 Numerical model

The masonry walls were simulated at prototype scale using 3D shell elements (S3) and a concrete damage plasticity (CDP) constitutive model in Abaqus, with building structures and material properties informed partly from the work of Yiu et al. (2017). The standard masonry wall (H8.5O19) has a mass density of 2423.5 kg/m^3, a Poisson's ratio of 0.2, a Young's modulus E of 3 GPa (E of elastic lintels taken as 3 times that of the masonry), infinite compressive strength, and a tensile strength of 50 kPa after which post-failure tensile stress increases with a positive gradient of 0.03 GPa (hardening failure).

In Yiu et al. (2017), a 215 mm thick masonry wall with openings rested on a 1 m wide strip foundation, resulting in a nominal stress of ~33.7 kPa. To achieve the same bearing stress, since the foundation width was limited to 2.66 m in prototype scale (i.e. 38 mm in model scale, mentioned above), the thickness of the numerical masonry walls was therefore scaled to 571 mm by an equal scaling ratio of 2.66 between foundation widths. The mesh size was ~0.41 m and the base of the walls consisted of 50 nodes.

In Abaqus, vertical displacements in the y-direction of the nodes along the wall base were controlled through a connection to the data exchange interface using a FORTRAN subroutine during centrifuge tests. The horizontal displacement in the x-direction and rotation about the z-direction were free.

2.3 Test plan

Four sets of tunnelling tests are summarised in Table 1, including one greenfield (GF), one standard two-storey masonry wall (H8.5O19), and two non-standard walls (H8.5O19E- and H8.5O19E+) with reduced (-) and increased (+) Young's modulus to reproduce the bending stiffness of one- and three-storey masonry walls. Note that the Young's modulus of lintels is always 3 times that of masonry.

Table 1. Test summary.

Label	*E* (GPa)	*EI* (GN m^2)	*GA* (GN/m)	Equivalent building
Greenfield	/	/	/	/
H8.5O19	3	52	1.9	two-storey
H8.5O19E-	0.7	12.1	0.4	one-storey
H8.5O19E+	6.2	107.5	3.9	three-storey

H: wall height; *O*: ratio of openings; *GA*: shear stiffness; *E*: Young's modulus of masonry; *EI*: bending stiffness.

2.4 Hybrid testing procedure

The dense sand (with a relative density of 90%) was prepared using the NCG automatic sand pourer. The

strongbox was positioned with its front acrylic wall facing downward, a temporary plate was fixed at the designated soil surface, and the tunnel was installed on the acrylic wall aligned in a vertical orientation. This allowed sand to be poured in the direction of the tunnel longitudinal axis (avoiding "shadowing" effects which would occur if the sand was poured with the tunnel aligned horizontally). After the sand filling, the back wall was attached to the strongbox, the strongbox was set up-right, the temporary plate was removed, and subsequent components were installed.

The numerical models underwent two analysis steps: the first involved the application of a gravity load to the walls within a single increment before centrifuge running, and the second step was the coupled simulation with the centrifuge model through the data exchange interface during centrifuge running, which required a substantial number of increments to cover the entire testing duration.

The centrifuge was spun up/down/up for "stabilisation cycles" (1-70-10-70-10-70 g) to reduce localised soil stress concentrations and improve test repeatability; the strip foundation was suspended from the load actuators without contacting the soil surface during this process. The foundation was then gradually lowered onto the soil surface at 70 g, and a preliminary load of 2 N was simultaneously applied to the seven loading positions on the foundation using a LabVIEW load-control program to ensure complete contact between the bottom of the foundation and the soil surface. The hybrid modelling process was then initiated, with the following steps:

S1. Initial loads determined by the geostatic wall self-weight were applied to the seven positions of the foundation concurrently in 25% increments, the foundation settlements (measured by LVDT) were initialised to 0, and the LabVIEW data exchange interface was then activated.
S2. A small increment of tunnel volume loss ($\triangle V_{l,t} \approx$ 0.1-0.2%) was manually initiated, which resulted in ground and foundation movements.
S3. The foundation settlements were transferred to the data exchange interface.
S4. The settlement data were fitted using a modified Gaussian curve (Vorster et al., 2005) and then interpolated (after scaling to prototype scale) to get the input node settlements along the wall base in Abaqus.
S5. The distortion and stress redistribution within the masonry walls were calculated in Abaqus based on the input node settlements; the change in settlements was always from the final settlement profile at the end of the preceding volume loss increment.
S6. The revised loads of the 50 nodes at the wall base were transferred to the data exchange interface and distributed (after scaling to model scale) to the 7 target concentrated (actuator) loads according to the relative node-to-actuator (cylinder) positions: n1-3[3]:a1, n4-13[10]:a2, n14-21[8]:a3, n22-29[8]:a4, n30-37[8]:a5, n38-47[10]:a6, n48-50[3]:a7, where n#-# indicates the node number in Abaqus, [#] is the number of nodes, and a# is the actuator number in the centrifuge model.
S7. The data exchange interface assessed whether a load balance state was achieved between the two model domains (i.e. the difference in each target concentrated (actuator) load and the load applied to the foundation in the previous cycle being less than 3 N). If yes, continue with step 8 with the current target concentrated loads, and wait for next tunnel volume loss (i.e. step 2). If not, continue with step 8 with revised target concentrated loads and repeat steps 3-8 (automatically).
S8. The concentrated loads from the data exchange interface were fed back to the strip foundation.

3 RESULTS AND ANALYSIS

3.1 Tensile deformation within buildings

Figure 3 presents the distribution of tensile strains within masonry buildings at $V_{l,t}$=2.2%, along with the corresponding characteristic tensile strain ε^t_{99} (the strain that is not exceeded in 99% of the total volume of the masonry wall, as adopted by Yiu et al. (2017)) and the areas of at least moderate damage (Mod. D., defined as ε^t >0.0015 according to Mair et al. (1996); results rounded to nearest integer value).

The areas of high tensile strains are observed to concentrate in the centre and lower part of the masonry buildings (i.e. beneath the door and near its top corners) and radiate to adjacent openings. The low-E building (H8.5O19E-) is most susceptible to tensile deformation or damage, with the highest ε^t_{99} and Mod. D. areas. Enhanced Young's modulus (H8.5O19E- vs H8.5O19 vs H8.5O19E+) reduces both the characteristic tensile strain ε^t_{99} and the area of Mod. D.. Considering the ratio between Young's modulus of the three buildings (0.2:1:2.1), the higher Young's modulus has a limited effect on reducing building tensile deformation whereas the lower Young's modulus increases the risk of building damage. The high Young's modulus of H8.5O19E+, compared to H8.5O19, results in a slightly more dispersed distribution of damage within the building, with more significant damage occurring around the two windows near the middle window on the upper layer and between the lintels of the lower layer windows; while the main area where damage is concentrated (i.e. around the door) is slightly smaller.

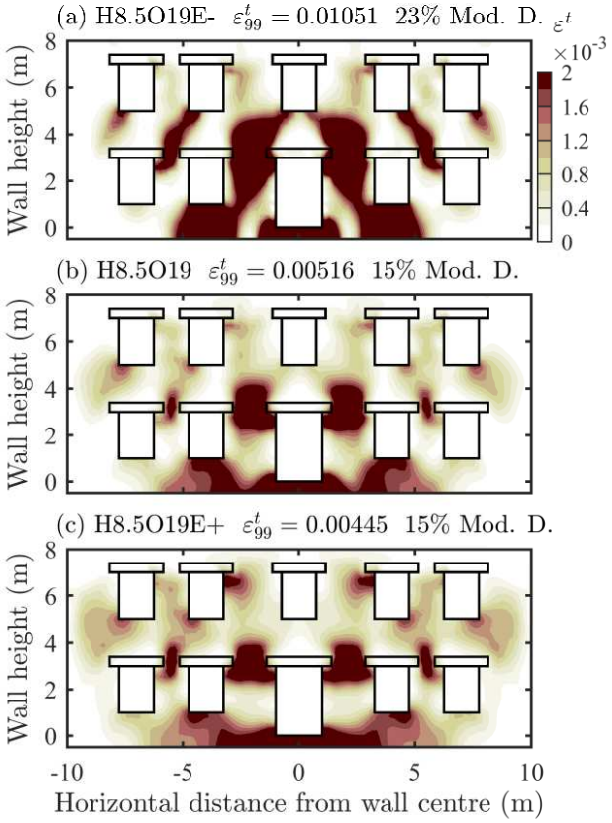

Figure 3. Changes in max principal strain (tensile strain) at $V_{l,t}$ = 2.2%.

3.2 Settlement at building base

Figure 4 shows the settlement curves at the base of different masonry buildings (fitted from LVDT data) and the greenfield surface settlement at $V_{l,t}$=2.2%. It is assumed that no gaps exist between the bottom of the foundation and the soil surface due to the relatively low foundation bending stiffness and the loading method, thus the building settlement curves in Figure 4 are regarded as the corresponding surface settlement troughs. The ground surface is shown to undergo higher settlements for the masonry building cases compared to the greenfield case.

Compared to the standard building H8.5O19, the higher Young's modulus case H8.5O19E+ (with the same building strength) reduces the settlements by 2-5 mm, however (somewhat unexpectedly) results in a slight increase in differential settlement. This counter-intuitive outcome occurs because of the non-linear response within the CDP model; the higher Young's modulus of H8.5O19E+ causes a more dispersed region of yield within the building, resulting in a reduction in effective secant stiffness of the building and the higher levels of distortion and differential settlement. The lower Young's modulus case H8.5O19E-, as expected, results in a significant increase in differential settlement, whereas the maximum settlement (i.e. at the centre of the settlement trough) is almost unchanged.

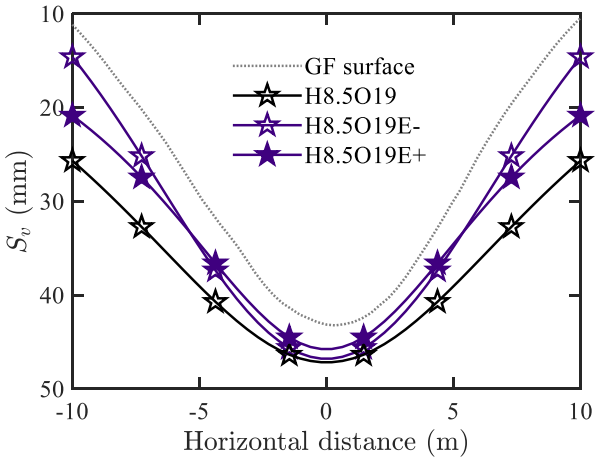

Figure 4. Settlement of building base and greenfield surface at $V_{l,t}$ = 2.2%.

3.3 Building deformation assessment

Figure 5 presents the deflection ratios of building and corresponding greenfield surface sagging and hogging areas against tunnel volume loss. Figure 6 shows the modification factors of building sagging and hogging deflection ratios based on the greenfield conditions (defined by Potts and Addenbrooke (1997)). The H8.5O19 test stopped at $V_{l,t}$=2.2% due to the lack of convergence in Abaqus; this issue was resolved in subsequent tests which allowed for higher volume losses to be achieved.

The deflection ratios in Figure 5 are approximately linearly related to the tunnel volume loss. The tested masonry buildings predominantly undergo sagging, with low-magnitude hogging deflection ratios. Compared to H8.5O19, the more flexible building (H8.5O189E-) shows higher sagging deflection ratios, close to that of the greenfield surface; the sagging deflection ratio of the stiffer building (H8.5O19E+) also slightly increases (for reasons explained earlier).

The modification factors of hogging deflection ratios (Figure 6) continue to increase until reaching 1 at $V_{l,t}$=3% (except H8.5O19 which stopped at $V_{l,t}$=2.2%; explained earlier). The sagging deflection ratio modification factors remain relatively constant after the tunnel volume loss exceeds 1%. The sagging deflection ratio modification factor of H8.5O19E+ is slightly higher than H8.5O19 (0.8 vs 0.7), while that of H8.5O19E- is approximately 1 (i.e. matches closely with greenfield conditions).

Deflection ratios and corresponding modification factors based on building base settlements reaffirm that enhancing Young's modulus has a limited impact on the overall deformation of the building, whereas reducing Young's modulus has a substantial effect.

Meanwhile, these results underscore the credibility of evaluating global building deformation (i.e. deflection ratios) through greenfield data.

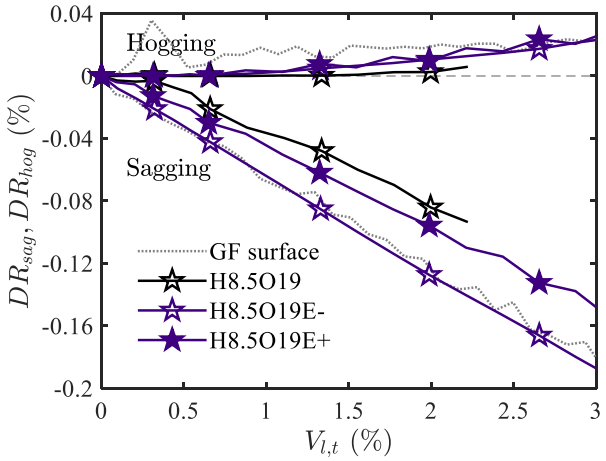

Figure 5. Building deflection ratios against tunnel volume loss.

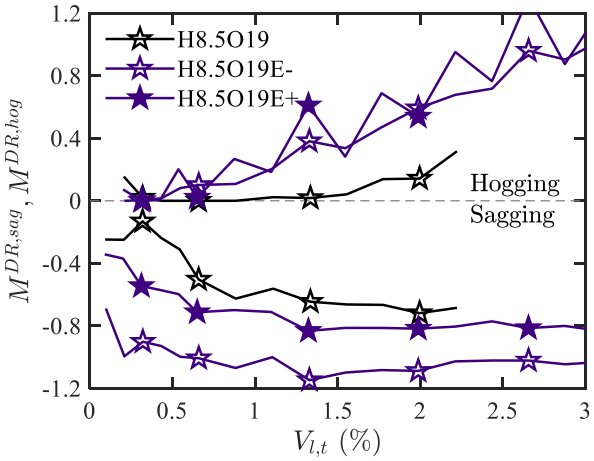

Figure 6. Modification factors of deflection ratios against tunnel volume loss.

4 CONCLUSIONS

This paper provided results from coupled centrifuge-numerical modelling (CCNM) tests on tunnelling beneath masonry walls with shallow strip foundations in dense sand and evaluated the effect of building Young's modulus within a CDP constitutive model on building deformation or damage.

High-level tensile strains (or damage levels of moderate and above) were observed to typically concentrate around the central lower door within masonry buildings. Compared with the standard masonry building case, higher Young's modulus, or enhanced bending stiffness, had the effect of dispersing high-level tensile strains more widely within the building, leading to increased differential settlement. Lower Young's modulus increased building flexibility, thus aligning settlement profiles, sagging and hogging deflection ratios, and their corresponding modification factors more closely to greenfield values, with a greater risk of tensile damage.

In this paper, the use of increased and decreased values of Young's modulus (replicating the bending stiffness of one- and three-storey walls within a two-storey masonry wall) gives insights into the impact of building material properties of masonry buildings in tunnelling scenarios.

ACKNOWLEDGEMENTS

The first author recognizes the financial support provided by the China Scholarship Council (CSC) and the University of Nottingham, UK.

REFERENCES

Farrell, R., Mair, R., Sciotti, A., and Pigorini, A. (2014). Building response to tunnelling. *Soils and Foundations*, 54(3): 269-279.

Mair, R., Taylor, R., and Burland, J. (1996). Prediction of ground movements and assessment of risk of building damage due to bored tunnelling. *Proceedings of Geotechnical Aspects of Underground Construction in Soft Ground*, 713-718.

Potts, D. and Addenbrooke, T. (1997). A structure's influence on tunnelling-induced ground movements. *Proceedings of the Institution of Civil Engineers-Geotechnical Engineering*, 125(2): 109-125.

Ritter, S., Giardina, G., Franza, A., and DeJong, M. J. (2020). Building deformation caused by tunneling: Centrifuge modeling. *Journal of Geotechnical and Geoenvironmental Engineering*, 146(5): 04020017.

Stanier, S. A., Blaber, J., Take, W. A., and White, D. J. (2016). Improved image-based deformation measurement for geotechnical applications. *Canadian Geotechnical Journal*, 53(5): 727-739.

Song, G. and Marshall, A. M. (2020). Centrifuge study on the influence of tunnel excavation on piles in sand. *Journal of Geotechnical and Geoenvironmental Engineering*, 146(12): 04020129.

Tang, C., Selvaraj, S. P., Heron, C. M., and Marshall, A. M. (2024). Coupled centrifuge-numerical modelling of shallow strip foundations. *Proceedings of Geotechnical Aspects of Underground Construction in Soft Ground*.

Yiu, W., Burd, H., and Martin, C. (2017). Finite-element modelling for the assessment of tunnel-induced damage to a masonry building. *Géotechnique*, 67(9): 780-794.

Vorster, T. E. B., Klar, A., Soga, K., and Mair, R. J. (2005). Estimating the effects of tunneling on existing pipelines. *Journal of Geotechnical and Geoenvironmental engineering*, 131(11): 1399-1410.